Lawrence Berkeley National Laboratory
LBL Publications

Title
Comparison of Model Predictions and Performance Test Data for a Prototype Thermal Energy Storage Module

Permalink
https://escholarship.org/uc/item/74b3t6h9

Journal
Journal of Energy Resources Technology, 143(2)

ISSN
0195-0738

Authors
Helmns, Dre
Carey, Van P
Kumar, Navin
et al.

Publication Date
2021-02-01

DOI
10.1115/1.4047607

Peer reviewed

Dre Helmns
Department of Mechanical Engineering,
University of California, Berkeley,
Berkeley, CA 94709
e-mail: ahelmns@berkeley.edu

Van P. Carey[1]
Department of Mechanical Engineering,
University of California, Berkeley,
Berkeley, CA 94709
e-mail: vpcarey@berkeley.edu

Navin Kumar
Department of Mechanical Engineering,
Texas A&M University,
College Station, TX 77843
e-mail: navinsubram@tamu.edu

Debjyoti Banerjee
Department of Mechanical Engineering,
Texas A&M University,
College Station, TX 77843
e-mail: dbanerjee@tamu.edu

Arun Muley
Boeing Research & Technology,
The Boeing Company,
Huntington Beach, CA 92647
e-mail: arun.muley@boeing.com

Michael Stoia
Boeing Research & Technology,
The Boeing Company,
Huntington Beach, CA 92647
e-mail: mike.stoia@boeing.com

Comparison of Model Predictions and Performance Test Data for a Prototype Thermal Energy Storage Module

Although model predictions of thermal energy storage (TES) performance have been explored in previous investigations, relevant test data that enable experimental validation of performance models have been limited. This is particularly true for high-performance TES designs that facilitate fast input and extraction of energy. In this paper, we present a summary of experimental tests of a high-performance TES unit using lithium nitrate trihydrate phase change material as a storage medium. Performance data are presented for complete dual-mode cycles consisting of extraction (melting) followed by charging (freezing). These tests simulate the cyclic operation of a TES unit for asynchronous cooling in a variety of applications. The model analysis is found to agree reasonably well, within 10%, with the experimental data except for conditions very near the initiation of freezing, a consequence of subcooling that is required to initiate solidification.
[DOI: 10.1115/1.4047607]

Keywords: energy conversion/systems, energy storage systems, energy systems analysis, heat energy generation/storage/transfer

Introduction

A number of earlier investigations have developed modeling methods for thermal storage [1–5]. Earlier analyses of phase change thermal storage have generally modeled specific details of heat transfer in the storage unit structure. Most are either strictly analytical, numerical, or experimental. Alkilani et al. conducted a theoretical investigation of the output air temperature of an indoor heater which utilizes a phase change material (PCM) heat exchanger [4]. Tay et al. used an ε-NTU method to generate an analytical solution to track latent heat transfer in a thermal storage device [5]. Ismail and Goncalves explored a two-dimensional model of a tube immersed in PCM [3]. By defining an appropriate control volume, the authors employ a finite difference scheme to characterize the thermal energy storage (TES) melt fraction, number of transfer units (NTU), and effectiveness. Other scientists combine mathematical analysis with computational research techniques. For example, Shamsundar and Srinivasan look at a three-dimensional shell and tube configuration both analytically and numerically (via finite difference) in which the working fluid temperature changes axially as heat is transferred from the PCM [1].

Some researchers have experimental data available with which to validate their work [6–10]. Bony and Citherlet developed a transient system model using the TRNSYS software environment to predict enthalpy as a function of temperature for several radial nodes within a cylindrical PCM heat exchanger. The authors subsequently validated this with experiments; by accounting for natural convection within the PCM, they were able to bring their initially predicted phase change end time (8 h) closer to what laboratory measurements demonstrated (3.5 h) [6]. Hosseini et al. conducted a similar experimental study on a single shell and tube heat exchanger with annular fins extending from the tube wall into the PCM. These researchers also used a computational fluid dynamics model to predict how the melt from propagates through an axial cross section of PCM near and between finned sections. While the average PCM temperatures were consistent between model and experiments, the model is not extended to predict anything about the working fluid [7]. Wu et al. consider a larger PCM storage tank integrated in a system with a heat pump and secondary heat exchanger. Globally, their simulation results agree very well (above 90% correlation) with experimental data. Yet, with the validation specific to the storage tank, the inlet and outlet temperatures are very close together, suggesting a low heat transfer rate between the working fluid and PCM. This is consistent with the longer time scale of the process [8]. Waser et al. employ a one-dimensional finite volume approach, discretizing a finned-tube heat exchanger into unit cells and analyzing the heat transfer locally. While their model predicts working fluid outlet temperature well, it also displays a similar problem as Wu's paper in that the inlet and outlet temperatures are very close to each other, perhaps due here to the outlet being looped directly back to the inlet [9]. The validity of this model is hard to gauge without additional experimental test conditions. Sun et al. conducted a very recent study using the Taguchi method to determine the optimum combination of operating conditions (inlet temperature, flow velocity, and inclination angle) to

improve TES performance. The error between their experimental melting time and model predicted melting time remained under 10% for the 25 tests conducted. It is important to note that the authors did not consider freezing and thus did not encounter the issue of subcooling which may reduce the accuracy of their model [10]. As is clear from these papers, the field can benefit from additional experimental data to validate the many closed-form solutions as well as computational results that researchers have generated. It is of particular importance to conduct studies for high-performance TES devices that undergo both melting and freezing processes in shorter time windows. Accurately predicting the working fluid temperature exiting a PCM heat exchanger is highly valuable for applications ranging from refrigeration and air conditioning to concentrated solar power plants. For these, a model needs to be robust enough predict the working fluid's outlet temperature for melting and freezing for a variety of operation conditions. The best models will consider secondary effects, including subcooling and natural convection.

The methodology and results that are presented in this paper are built upon a larger body of work from this group over the last several years [11–16]. The first of these contains the derivation of a non-dimensional framework developed in order to analyze thermal energy storage technology [11]. From there, efforts were focused on quantifying the space and time varying conductance inherent in the transient melting and freezing processes of latent thermal storage. That work was used to justify the use of an average conductance in future modeling; the effectiveness of high-performance devices is not sensitive to variations in conductance [12]. Additional work has been done since then to determine a simpler relation for average conductance as a function of the melt fraction [13]. In tandem, the TES device was examined in the context of a larger sub-system, consisting of external heat exchangers used to input and reject heat to and from the storage. This problem was mathematically challenging by introducing spatially varying initial conditions (due to the nature of cyclic melting and freezing processes) as well as a transient boundary condition (for the varying working fluid temperature from the heat exchangers) [14]. The system equations derived in this paper were applied to model the performance of a power plant using TES for asynchronous cooling of a Rankine cycle steam condenser [15]. This paper was expanded to demonstrate the economic viability of thermal storage for arid climates [16]. A major remaining piece in this body of work is to validate the numerical framework used in our previous explorations. In our earlier studies, we had little to no experimental data with which to validate our numerical model. The culmination of previous work provides a great basis for comparison with experimental testing of a TES device. Thus, the primary objective of this paper is to compare recent modeling to new experimental data. We aim to address the gaps in the existing literature by modeling a high-performance TES device that undergoes melting and solidification in shorter time windows and accurately predicts the outlet working fluid temperature of the heat exchanger for time-varying operating conditions.

Methodology

Three differential equations govern the temperature and melt fraction fields within a thermal energy storage device. Thermal energy is advected by the working fluid and enters or leaves the storage matrix through the channel wall

$$\frac{\partial T_w}{\partial t} = -\left(\frac{\dot{m}}{\rho_w A_c}\right)\frac{\partial T_w}{\partial z} + \frac{U s_w}{\rho_w A_c c_{p,w}}(T_e - T_w) \tag{1}$$

$$\frac{\partial T_e}{\partial t} = \frac{U s_w}{\rho_s c_{p,s} \nu'}(T_w - T_e); \quad \frac{\partial x_e}{\partial t} = 0 \tag{2}$$

for $T_e \neq T_m$ (sensible heat transfer) and $x_e = 0$ or $x_e = 1$

$$\frac{\partial x_e}{\partial t} = \frac{U s_w}{\rho_s h_{ls} \nu'}(T_w - T_e); \quad \frac{\partial T_e}{\partial t} = 0 \tag{3}$$

for $T_e = T_m$ (latent heat transfer) and $0 < x_e < 1$.

These equations are converted to a non-dimensional framework, as is typically done for heat exchanger analysis (e.g., effectiveness-NTU). Due to the complex nature of phase change physics, we require several dimensionless groups to predict performance. The differential equations within the TES device are non-dimensionalized using the following definitions:

$$\theta = \frac{T_e - T_{min}}{T_{max} - T_{min}}, \quad \phi = \frac{T_w - T_{min}}{T_{max} - T_{min}} \tag{4}$$

$$\hat{z} = \frac{z}{L}, \quad t^* = \frac{t}{t_{res}}, \quad t_{res} = \frac{\rho_w A_c L}{\dot{m}} \tag{5}$$

These non-dimensional equations scale φ, θ, and x_e such that each of these variables takes on values between 0 and 1

$$\frac{\partial \phi}{\partial t^*} = -\frac{\partial \phi}{\partial \hat{z}} + N_{tu}(\theta - \phi) \tag{6}$$

$$\frac{\partial \theta}{\partial t^*} = N_{tu} R_{we}(\phi - \theta); \quad \frac{\partial x_e}{\partial t^*} = 0 \tag{7}$$

for $\theta \neq \theta_m$ and $x_e = 0$ or $x_e = 1$

$$\frac{\partial x_e}{\partial t^*} = N_{tu} R_{we} \text{St}_{io}(\phi - \theta); \quad \frac{\partial \theta}{\partial t^*} = 0 \tag{8}$$

for $\theta = \theta_m$ and $0 < x_e < 1$.

Relevant dimensionless parameters are formed to concisely write the governing equations. Two of the non-dimensional groups are similar to those that result from compact heat exchanger (CHX) analysis, with the addition of a third that accounts for latent heat transfer. The number of transfer units, N_{tu}, relates the heat transfer into the matrix to that advected along the flow. It is critical for design because it encapsulates the conductance, UA, which is inherently dependent on the device configuration. The second parameter, R_{we}, is the ratio of thermal capacities between the working fluid and matrix element and thus is dependent on the materials selected. The third parameter, the Stefan number, St_{io}, relates the relative importance of sensible heat transfer to latent heat transfer. This captures the operating conditions, namely, the temperature range in which the thermal energy storage is used. For the previously outlined purpose to transfer energy via latent heat transfer, the Stefan number will be quite small. These dimensionless groups are defined as

$$N_{tu} = \frac{U s_w L}{\dot{m} c_{p,w}}, \quad R_{we} = \frac{\rho_w c_{p,w} A_c}{\rho_s c_{p,s} \nu'}, \quad \text{St}_{io} = \frac{c_{p,s}(T_{max} - T_{min})}{h_{ls}} \tag{9}$$

Typical values of the dimensionless numbers for the energy applications considered here might be

$$N_{tu} = \mathcal{O}(10^1), \quad R_{we} = \mathcal{O}(10^0), \quad \text{St}_{io} = \mathcal{O}(10^{-1}) \tag{10}$$

These will be calculated from TES device geometry, thermophysical properties, and transport parameters.

Numerical Framework. In order to solve the differential equations numerically, we use a first-order accurate finite difference approximation, employing the upwind and forward Euler discretization methods, respectively. The temperature and melt fraction fields in the storage matrix are determined using these equations. This working fluid temperature, φ, is dictated by

$$\phi_j^{n+1} = \phi_j^n + \Delta t^*[N_{tu}(\theta_j^n - \phi_j^n)] - \frac{\Delta t^*}{\Delta \hat{z}}[\phi_j^n - \phi_{j-1}^n] \tag{11}$$

This equation is first-order in time and space, necessitating a boundary and an initial condition. The working fluid exchanges heat with phase change material in the storage matrix which undergoes both sensible and latent heat transfer depending on the temperature of each discrete node. Sensible energy storage occurs when a cell containing PCM at position $j\Delta\hat{z}$ and time $n\Delta t^*$ is not at its melt

temperature, θ_m. The storage matrix temperature at the next time-step can be determined via

$$\theta_j^{n+1} = \theta_j^n + \Delta t^*[N_{tu}R_{we}(\phi_j^n - \theta_j^n)]; \quad x_{e,j}^{n+1} = x_{e,j}^n \quad (12)$$

for $\theta_j^n \neq \theta_m$ and $x_{e,j}^n = 0$ or $x_{e,j}^n = 1$.

If Eq. (12) would result in the temperature at the next time-step, $n+1$, to pass the melt temperature, then θ_j^{n+1} is set to θ_m and latent energy storage begins, with change in melt fraction calculated from Eq. (13):

$$x_{e,j}^{n+1} = x_{e,j}^n + \Delta t^*[N_{tu}R_{we}\text{St}_{io}(\phi_j^n - \theta_j^n)]; \quad \theta_j^{n+1} = \theta_j^n \quad (13)$$

for $\theta_j^n = \theta_m$ and $0 < x_{e,j}^n < 1$.

The equations governing the storage matrix temperature and melt fraction are first-order in time but have no spatial derivative. As such, only one boundary condition is required to solve these coupled first-order differential equations. In $\hat{z}$, we non-dimensionalize the time-varying working fluid inlet temperature, T_{wi}, to write the boundary condition in its dimensionless form

$$\text{At} \ \hat{z} = 0: \quad \phi_{j=1}^n = \phi_{wi}(t^*) \quad (14)$$

for $t^* > 0$.

Initial conditions on temperatures, ϕ and θ, and melt fraction, x_e, are also required for the entire domain. At the beginning of extraction, we might expect the PCM in the device to be completely frozen at the cold system temperature, corresponding to dimensionless values of 0 for ϕ, θ, and x_e. Conversely, after a complete melting process ending at the hot system temperature, the initial conditions for re-freezing the device might correspond to dimensionless values of 1. That said, these can represent any distribution desired as in Eq. (15):

$$\text{At} \ t^* = 0: \quad \phi_j^{n=1} = \phi_0(\hat{z}), \quad \theta_j^{n=1} = \theta_0(\hat{z}), \quad x_{e,j}^{n=1} = x_{e,0}(\hat{z}) \quad (15)$$

for $0 \leq \hat{z} \leq 1$.

These initial and boundary conditions can be spatially uniform and temporally steady. To capture physical complexity, the initial conditions can be modified to match the end and beginning of subsequent processes; the boundary condition can be adjusted to capture time-varying conditions. The temperature and melt fraction fields should be resolved spatially and temporally until the melting or freezing process end time, t_{end}^*, is reached. In order to determine device performance at t_{end}^*, the following equation should be used to evaluate effectiveness, ε_{tes}:

$$\varepsilon_{tes,ext} = \frac{\sum_{\hat{z}=0}^1 x_e(t_{end}^*, \hat{z})}{\sum_{\hat{z}=0}^1 x_{e,max}(t^*, \hat{z})} \quad \text{where } x_{e,max} = 1 \quad (16)$$

for the extraction (melting) process

$$\varepsilon_{tes,char} = \frac{\sum_{\hat{z}=0}^1 1 - x_e(t_{end}^*, \hat{z})}{\sum_{\hat{z}=0}^1 1 - x_{e,min}(t^*, \hat{z})} \quad \text{where } x_{e,min} = 0 \quad (17)$$

for the charging (freezing) process.

The storage process, which may occur between extraction and charging processes, is not characterized as having an effectiveness (because no energy is added or removed from the device). For the experimental testing of the prototype described in the Experiment Design section, charging immediately followed extraction; no storage took place. The effectiveness for either extraction or charging has the functional relationship

$$\varepsilon_{tes} = \varepsilon_{tes}(t^*, N_{tu}, R_{we}, \text{St}_{io}) \quad (18)$$

In addition, the energy capacity of the TES can be calculated according to

$$E_{cap} = \rho_{\text{PCM}} \nu' L h_{ls} \varepsilon_{tes} \quad (19)$$

Experiment Design

The remainder of this paper is dedicated to applying the methodology and numerical framework described above to a 100 kJ TES device. A CHX was fabricated and assembled by a commercial vendor (Allcomp Inc., City of Industry, CA) and subsequently filled with a phase change material. The working fluid, i.e., the heat transfer fluid (HTF), was used to melt and solidify the PCM in repeated thermal cycles involving complete solidification and incomplete melting; this technique is called the "cold finger" approach. The TES has an offset fin configuration on the working fluid side and aluminum porous fins in the storage matrix. The device has five flow channels for HTF flow and four hermetically sealed channels with encapsulated PCM. Experimental testing of this prototype was performed at Texas A&M.

Device Geometry. The TES prototype consists of stacked rectangular sections, alternating between flow passages and storage matrix sections. The unit was fabricated using mature fin forming and vacuum brazing processes. The liquid-side heat transfer surface is a 3000 series aluminum offset fin, while the PCM-side utilizes a high-density plain fin formed from 5056-O aluminum wire mesh. The TES HX core is comprised of four PCM cavities that are sandwiched between five liquid cooling passages. Header caps were bonded to the TES HX core to support cyclic testing. Note that the assembly of a mass produced TES unit would employ a more robust joining technique (e.g., welding).

The HTF region of the TES had an offset fin density of 22 fins/in.; the offset fin configuration was selected due to its high surface area. The heat exchanger and offset fins were manufactured using Al-3003 material. The PCM channels are brazed with aluminum foam (porous fin). The aluminum porous fin was formed by folding a porous aluminum thread (wire) based fabric sheet. The purpose of the aluminum foam is to enhance the effective thermal conductivity of PCM.

The design allowed the center PCM channels to have higher effective heat transfer area compared with top and bottom PCM channels as illustrated in Fig. 1. This resulted in faster charging and discharging in the center PCM channels in comparison to the top and bottom PCM channels.

Specific details of the design are summarized in Table 1. Of particular interest is the void fraction which greatly impacts the effective properties that form the dimensionless parameters in the governing equations.

Thermophysical Properties. There are four types of phase change materials that might be used in this type of application: organic paraffins, organic nonparaffins, inorganic salt hydrates, and inorganic metal eutectics [17]. Organic paraffins have a high latent heat of fusion but are derived from petroleum. Organic nonparaffins are not derived from petroleum but tend to be very expensive. Inorganic salt hydrates are very cheap but unfortunately are unstable over repeated cycling. All of the above suffer from low thermal conductivity which makes the process of inputting or removing energy from the PCM more difficult. This can be remedied with an inorganic metal eutectic which has excellent thermal conductivity but a lower latent heat of fusion than other materials. When selecting an appropriate PCM among these, affordability is highly important. With all of these factors in mind, the material chosen for the prototype was lithium nitrate trihydrate, a salt hydrate that has been optimized to better handle transient cycling. Anhydrous lithium nitrate salt powders were procured commercially from Beantown Chemical, NH with purity greater than 99%. Thermophysical properties are shown in Table 2 [18].

The amount of PCM inserted into the TES was 474 g. The filling rate of PCM does not affect the calculation nor the experimental results. Instead, we are concerned with the energy capacity of the PCM contained within the TES. The latent heat of lithium nitrate trihydrate was measured in this study to be 278 kJ/kg using the
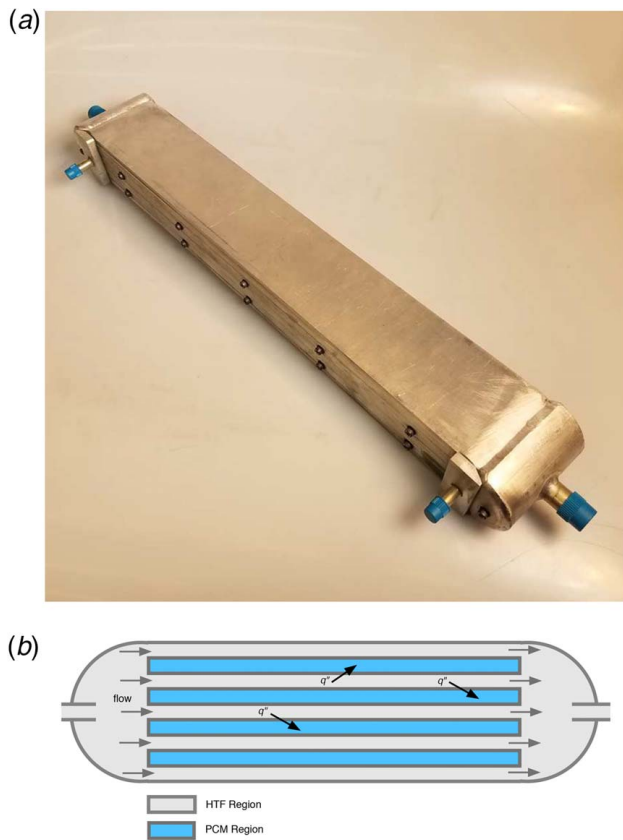
(a)

(b)

☐ HTF Region
☐ PCM Region

Fig. 1 Photograph and schematic (not to scale) illustrating heat flux (q'') from the hot HTF region into the PCM region during the melting process

Table 1 Thermal energy storage prototype geometry

Length of TES device (L)	0.407	m
Wetted perimeter of flow passage (s_w)	9.42×10^{-2}	m
Cross-sectional area of flow passage (A_c)	8.97×10^{-5}	m^2
Matrix volume per unit flow length (v')	1.99×10^{-4}	m^2
Number of flow passages (n_w)	5	
Number of storage matrix sections (n_s)	4	
Void fraction in storage matrix (ε_s)	0.729	

Table 2 PCM properties: lithium nitrate trihydrate

Thermal conductivity (k_{PCM})	0.584	W/(m K)
Density (ρ_{PCM})	1500	kg/m^3
Specific heat ($c_{p,PCM}$)	2910	J/(kg K)
Latent heat of fusion (h_{ls})	278	kJ/kg
Melting temperature (T_m)	30	°C

T-History method. Thus, the theoretical energy storage capacity of the device was rated to be 130 kJ which differs slightly from the rated capacity of 100 kJ.

Note: The melt temperature experimentally deviates from this single value, T_m, due to the subcooling or superheating required to initiate phase change.

Other properties that are not solely associated with latent heat transfer can be adjusted by adding a metal mesh to the storage matrix. As the thermal conductivity of lithium nitrate trihydate is quite low, a metal matrix structure is required to effectively conduct heat through the storage matrix. Any high conductivity material would be suited for this application, but the low cost of aluminum makes it ideal for this technology. Its properties are shown in Table 3.

Table 3 Metal mesh properties: aluminum 5056

Thermal conductivity (k_m)	117	W/(m K)
Density (ρ_m)	2640	kg/m^3
Specific heat ($c_{p,m}$)	910	J/(kg K)

Aluminum is a cheap option that is chemically compatible with the PCM. Metal pathways are ideal for spreading the thermal energy away from the channel wall toward the melt front. They enhance the effective properties (conductivity, density, and specific heat) of the storage matrix which are calculated according to

$$\bar{p} = p_m(1 - \varepsilon_s) + p_{PCM}\varepsilon_s \quad (20)$$

The effective properties determined from Eq. (20) are summarized in Table 4.

The thermophysical properties of the working fluid are also necessary in order to solve the governing equations. The experiments were conducted with pure de-ionized water. Its properties were taken at the inlet temperatures for extraction and for charging, respectively.

The ranges in Table 5 reflect the values associated with the cold and hot fluid inlet temperatures.

Experimental Apparatus and Procedure. The melt front and freeze front of the PCM in the top and center channels were monitored by embedding thermocouples at predefined locations. The predefined locations correspond to 10%, 30%, 50%, 70%, and 90% melt fractions along the axial directions as illustrated in Fig. 2. The temperature of the HTF was measured at the inlet and outlet plenum of the compact heat exchanger.

Two different HTF flow configurations (A and B) were explored during solidification and melting experiments to study the efficacy of cold finger techniques. Cold finger techniques involve thermal cycling protocols with complete solidification and incomplete melting of the PCM samples under consideration. The incomplete melting protocols enable a residue of PCM crystals to remain in the PCM sample—which in turn act as nucleators by promoting nucleation. Prior studies have shown that having an un-melted portion of the PCM, like residue crystals, provides better efficacy for promoting nucleation than that of heterogeneous additives for the same purpose. The result is that freezing can initiate with subcooling less than 1 °C.

To realize the full effectiveness of the cold finger techniques, the experiments were designed for the flow of HTF in to the CHX to be bidirectional. In configuration A, the flow of HTF during melting is from left to right, whereas during solidification, the flow of HTF was reversed to flow from right to left (i.e., opposite direction during charging and discharging). In configuration B, the flow of HTF during melting and solidification is from left to right (i.e., same direction during charging and discharging). For the complete melting and freezing tests, the flow direction matched configuration B, with both HTF flows in the same direction as shown in Fig. 2.

Table 4 Effective properties: storage matrix

Effective thermal conductivity (k_s)	32.1	W/(m K)
Effective density (ρ_s)	1810	kg/m^3
Effective specific heat ($c_{p,s}$)	2370	J/(kg K)

Table 5 Working fluid properties: water

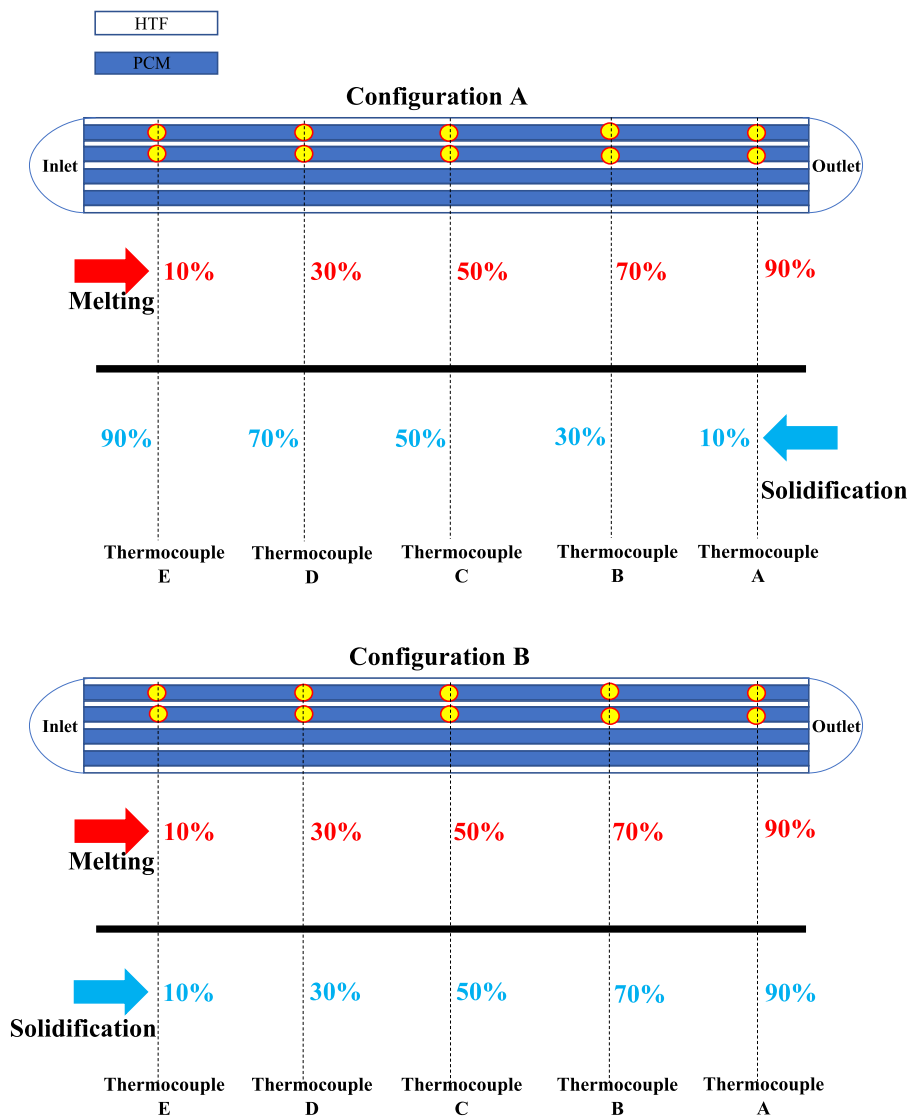|		
Thermal conductivity (k_w)	0.608–0.623	W/(m K)
Density (ρ_w)	994–997	kg/m^3
Specific heat ($c_{p,w}$)	4090–4130	J/(kg K)

Fig. 2   Schematic showing the location of thermocouples inserted in the CHX to monitor temperature during charging and extraction for two different flow configurations: melting and solidification in the opposite or same working fluid flow directions

The cold finger experiments were designed for the melting to proceed until 90% of the total latent heat (i.e., the total energy storage capacity) was utilized, thus allowing about 10% of the remaining PCM to be un-melted and remain in solid phase as dispersed crystals or unused energy storage capacity. Thus, storage capacity is sacrificed marginally to enable more reliable operation by enhancing the efficacy of the residual crystals (un-melted portion of the PCM) to initiate the nucleation and subsequent propagation of the solidification front in the melted phase of the PCM. The variation in flow direction was manipulated with three-way valves with different valve configurations for melting and solidification.

The top PCM channel was used as the reference for monitoring the propagation of the melting front. The PCM charging and discharging temperature conditions were achieved using two different water baths. The hot water bath was maintained slightly above phase transition temperature (i.e., 35 °C) using a chiller unit, and the cold water bath was maintained at a temperature below phase transition temperature (i.e., 25 °C). The two water baths (chiller units) were purchased from Cole-Parmer (Model: Polystat cooling/heating circulating baths, 2C15). Data were collected to indicate when 90% of the PCM was melted by hot HTF pumped

into the TES from the hot water bath. At that point, the valves were switched to pumping of cooling HTF (freezing) from the cold water bath. At this switch point, the PCM matrix section temperature recorded by the thermocouple at the 90% melt fraction location of the top channel reached 30.5 °C. This allowed for maximization of the storage capacity and enabled the implementation of the cold finger technique. The thermocouples utilized in the temperature measurements were K-type (1/16″ diameter) with hydrothermic sheathed tips (Sheathing Material: SS 316, and Manufacturer: Temprel, OH). The tip of the thermocouple is located centrally along the width of the heat exchanger (1.5″ from the edge) as shown in Fig. 3. The thermocouples were calibrated in a water bath from 10 °C to 40 °C at an interval of 0.5 °C using an NIST Standard thermometer (least count: ±0.25 °C and calibration uncertainty of 0.8%). After calibration, the uncertainty of the thermocouples was determined to be ±0.25 °C to ±0.35 °C.

A high-speed data acquisition (DAQ) system was used for recording the temperature measured by the thermocouples. The DAQ consists of an NI SCXI 1000 Chassis and an NI SCXI-1303 board. The temperature measurements were performed at 1 Hz frequency (i.e., 1 reading/s). The least count accuracy of the DAQ system was 0.003 °C; therefore, the uncertainty from the DAQ
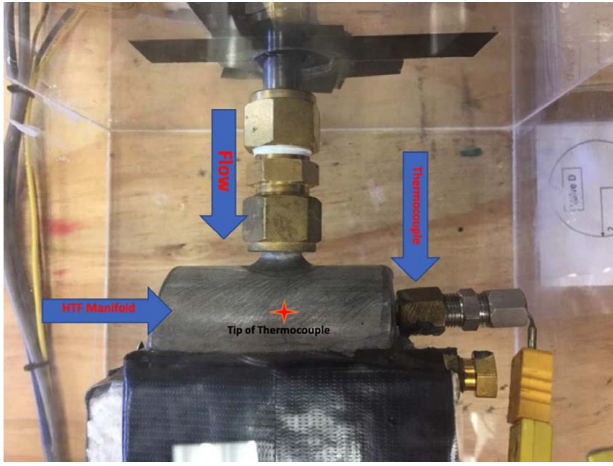
Fig. 3 Photograph of thermocouple location centered in inlet HTF flow manifold

can be considered negligible. Simultaneously, the voltage measurement from the flowmeter was acquired using an NI USB 9162 DAQ at 1 Hz frequency. The HTF volumetric flowrate in the system was measured by an Omega FLR 1000 series flowmeter (S/N 10,981) which was calibrated for 0.2–2 l/min (purchased from OMEGA).

The thermal performance of the TES was analyzed by varying (a) the flowrate of the HTF during charging and discharging and (b) the inlet temperature of the HTF during charging and discharging. The volumetric flowrate was varied between 3 and 5 gallons/h (0.003–0.005 kg/s) and the HTF inlet temperatures tested during melting were 33–37.4 °C. Similarly, during solidification, the HTF inlet temperature was varied between 20 and 26 °C. Specific test temperatures and flowrates used in the model are specified in Table 7. The design condition for the compact heat exchanger was 3 gallons/h with an inlet temperature of 37.0 °C during melting (discharging) and 25.5 °C during freezing (charging). The experiments were repeated two times with and without insulation to ensuring repeatability of the experiments. The insulated and un-insulated cases allowed for the comparison of parasitic heat loss to the environment during the melting and solidification process.

The experimental steps are listed as follows:

(1) Initially solidify (charge) PCM with HTF at a cold inlet temperature of ∼25.5 °C at ∼3 gallons/h,
(2) Close the cold HTF control valve and turn valves to direct the hot HTF at ∼37.0 °C at ∼3 gallons/h,
(3) Open the hot HTF control valve and melt (discharge) to the desired melt fraction of PCM—90% for cold finger or 100% for complete, and
(4) Close the hot HTF flow control valve and turn valves to direct the cold HTF to completely solidify the PCM.
(5) Repeat steps (2) through (4) above to ensure repeatability with varying HTF mass flowrate and inlet temperature.

The efficacy of cold finger techniques was experimentally validated in this TES. To summarize, the cold finger protocol consisted of 90% melting of PCM—leaving 10% of PCM as solid crystals prior to complete solidification of PCM. The flow direction of the HTF was varied to study the sensitivity of flow direction on solidification and the subcooling required to initiate freezing. While discussion of the cold finger technique is compelling, it is out of the scope of this work and not included in the model validation presented in the Results section. Further information on dynamic nucleation of subcooled phase change materials can be found in the literature [19,20].

The temperature difference of the HTF between inlet and outlet was computed as follows:

$$\Delta T_{\mathrm{HTF}} = T_{\mathrm{outlet}} - T_{\mathrm{inlet}} \qquad (21)$$

where T_{outlet} is the HTF temperature measured at the outlet port of the heat exchanger and T_{inlet} is the inlet temperature measured at the inlet port of the heat exchanger. The measurement uncertainty of the ΔT_{HTF} was estimated by using the following equation:

$$u_{\Delta T} = \left[\left(\frac{\partial \Delta T_{\mathrm{HTF}}}{\partial T_{\mathrm{outlet}}} \right)^2 (u_{T_{out}})^2 + \left(\frac{\partial \Delta T_{\mathrm{HTF}}}{\partial T_{\mathrm{inlet}}} \right)^2 (u_{T_{in}})^2 \right]^{1/2} \qquad (22)$$

where u is the statistical uncertainty for each variable. The calibrated uncertainty of thermocouples was determined to be ± 0.35 °C between 10 °C and 40 °C. The nominal value for the measurement uncertainty for ΔT_{HTF} is therefore estimated to be ± 0.49 °C. This corresponds to a temperature measurement uncertainty of 3.0%. However, due to bending of the thermocouples during the experiment, we estimate the uncertainty to be 2.0% higher. The experimental measurement uncertainty is summarized in Table 6.

The experimental effectiveness (ε_{exp}) of the TES was determined using the following equation:

$$\varepsilon_{exp} = \frac{T_{\mathrm{inlet}} - T_{\mathrm{outlet}}}{T_{\mathrm{inlet}} - T_{\mathrm{PCM}}} \qquad (23)$$

where T_{PCM} is the local temperature of the PCM. The thermal storage capacity of the heat exchanger at any instant was calculated by using Eq. (24), based on the measurements of the HTF temperature values and mass flowrates:

$$E = m_w c_{p,w} \Delta T_{\mathrm{HTF}} \qquad (24)$$

where m_w is the total mass flow over a short duration of the experiment and $c_{p,w}$ is the specific heat capacity of the HTF. The cumulative values of the instantaneous thermal energy storage can be used to estimate the total energy storage capacity of the TES for either the charging or discharging portion of the cycle. The instantaneous power, P, for the TES was calculated as follows:

$$P = \dot{m}_w c_{p,w} \Delta T_{\mathrm{HTF}} \qquad (25)$$

where $\dot{m}_w$ is the mass flowrate at any instant. The instantaneous power can be integrated over a specified time period and divided by the total time period in order to obtain the average power over the chosen time period. The Stefan number (St) at any instant can be estimated using the following equation:

$$\mathrm{St} = \frac{(\mathrm{Sensible\ heat})}{(\mathrm{Latent\ heat})} = \frac{c_{p,w} \Delta T_{\mathrm{HTF}}}{h_{ls}} \qquad (26)$$

where h_{ls} is the latent heat of fusion of the phase change material.

Table 6 Experimental measurement uncertainty

Temperature measurement uncertainty	5.0%
Flowmeter measurement uncertainty	4.3%

Table 7 Thermal energy storage operating parameters

Average mass flowrate for extraction ($\dot{m}_{ext}$)	3.44×10^{-3}	kg/s
Average mass flowrate for charging ($\dot{m}_{char}$)	3.56×10^{-3}	kg/s
Average inlet temperature for extraction ($T_{wi,ext}$)	36	°C
Average inlet temperature for charging ($T_{wi,char}$)	26	°C

Model Transport Parameters. The transient flowrates for extraction and charging were provided with TAMU experimental data. Due to a 4.3% uncertainty reported in flowrate measurements, a slightly lower time-averaged flowrate was input into the numerical model to account for any hydrodynamic losses. The total mass flow-rate, given in Table 7, is assumed to be distributed equally among the five flow passages in the device.

The working fluid in all tests came in at a relatively constant inlet temperature after being ramped up or down to that, respectively. The properties of the working fluid were assumed to be constant throughout a given process and determined based on the time-averaged water inlet temperature.

Calculating Conductance. With the device geometry, thermophysical properties, and transport parameters specified, a convective heat transfer coefficient can be determined via correlation. The flow passages consist of offset fins, giving a Colburn-j type relation:

$$j = 0.6522 * \text{Re}^{-0.5403} \left(\frac{s}{h_f}\right)^{-0.1541} \left(\frac{t_f}{l_f}\right)^{0.1499} \left(\frac{t_f}{s}\right)^{-0.0678}$$

$$\left(1 + 5.269 * 10^{-5}\text{Re}^{1.340} \left(\frac{s}{h_f}\right)^{0.504} \left(\frac{t_f}{l_f}\right)^{0.456} \left(\frac{t_f}{s}\right)^{-1.055}\right)^{-0.1} \tag{27}$$

where Re is the Reynolds number of the flow, s is the spacing between fins, h_f is the height of the fins, t_f is the thickness of the fins, and l_f is the length of the fins.

The Colburn-j factor is used to calculate the Stanton number, Sta, which is subsequently used to calculate the Nusselt number, Nu, and from there, solve for the convective heat transfer coefficient, h.

$$\text{Sta} = \frac{j}{\text{Pr}^{2/3}}, \quad \text{Nu} = \text{StaRePr}, \quad h = \frac{k_w \text{Nu}}{D_h} \tag{28}$$

With h, the overall heat transfer coefficient, U, can be found. Based on geometry, a stability analysis is performed for the PCM matrix enclosure to determine whether or not natural convection occurs. A fluid heated from the bottom is stable provided its Rayleigh number is below a critical value. The Rayleigh number has a cubic dependence on the characteristic length. For the geometry given in Table 1, natural convection is not present. As noted in the introduction, previous work has been used to derive U [12,13]. The more elegant of these results will be used, namely, that the overall heat transfer coefficient, U, can be found from the device geometry (A_t, A_w, h_s), thermophysical properties (k_s), convective coefficient, h, and the melt fraction, x_e, which is a function of position in the device as well as time

$$U_{ext} = \left[\frac{1}{h(A_t/A_w)} + \frac{h_s}{2k_s}x_e\right]^{-1} \tag{29}$$

where $A_t/A_w = (\eta_{fin}h_f + s)/(s + t_f)$ including the offset fin efficiency and h_s is the height of the storage matrix sections.

A key finding from both studies of conductance was that an average U could be used in place of a spatially and temporally varying one. To be sure that this was also the case for the prototype experiments, we applied a quasi-steady treatment of the variation of U with x_e and compared our results to constant conductance. As the conductance is quite high, we see no measurable difference in the fluid outlet temperature predicted. Thus, an average conductance is suitable for modeling the TES. In order to average Eq. (29), we integrate over the range of x_e encountered during the melting

process

$$\overline{U}_{ext} = \frac{1}{x_{ef}} \int_{x_{e,i}=0}^{x_{ef}=1} \left[\frac{1}{h(A_t/A_w)} + \frac{h_s}{2k_s}x_e\right]^{-1} dx_e \tag{30}$$

After integrating over melt fraction and normalizing by the final value, we find that

$$\overline{U}_{ext} = \frac{2k_s}{h_s}\ln\left[1 + \frac{h_s}{2k_s}h(A_t/A_w)\right] \tag{31}$$

This gives a value for $\overline{U}_{ext}$ that falls between the convective heat transfer coefficient (h) and the steady-state value reached at the end of melting that U asymptotes to when the PCM melt front reaches the adiabat between flow passages. The key term in the variable U expression, x_e, can be interpreted as a proxy for the growing distance between the channel wall and the melt front. This term is the dominant thermal resistance in the problem due to the high efficiency of the working fluid side heat transfer. By extrapolating this simple model to freezing, we predict the values given in Table 8 for TES conductance.

This average overall heat transfer coefficient is subsequently used to calculate N_{tu}, the number of transfer units, required to solve the non-dimensionalized set of equations that comprise the numerical framework. The complete set of parameters in the three governing equations would be non-dimensionalized according to Eq. (9) giving the values in Table 9.

Results and Discussion

Table 9 enables us to proceed with the solution of the differential equations (11)–(13) with the boundary condition given by Eq. (14) and initial conditions from Eq. (15). The boundary condition is a time-varying working fluid inlet temperature, shown in red in Figs. 4–6. The initial condition is taken to be completely frozen at the start of melting (0 min), while the spatial distribution at the end of extraction (~34 min) serves as the initial condition for the freezing process. Solving the differential equations with these conditions provides spatially and temporally resolved temperature and melt fraction fields. The grid size used to solve the equations for the results presented in this paper are $\Delta\hat{z} = .005$ and $\Delta t^* = .00025$.

Note: For extraction, the melt temperature was taken to be 29.66 °C, and for charging, the melt temperature was taken to be 29.5 °C.

These values are well within the range predicted by experiments.

Four experimental tests were conducted at TAMU. Two of these consisted of complete melting and freezing, while the others examined incomplete melting followed by freezing. This was done in an effort to combat the poor nucleation rates that resulted once the entire PCM domain was liquid. While all four tests are important, those with complete melting and freezing are most relevant for

Table 8   Averaged overall heat transfer coefficient, $\overline{U}$

Run 1 Ext	2990	W/(m² K)
Run 1 Char	2880	W/(m² K)
Run 2 Ext	2980	W/(m² K)
Run 2 Char	2930	W/(m² K)

Table 9   Thermal energy storage dimensionless variables

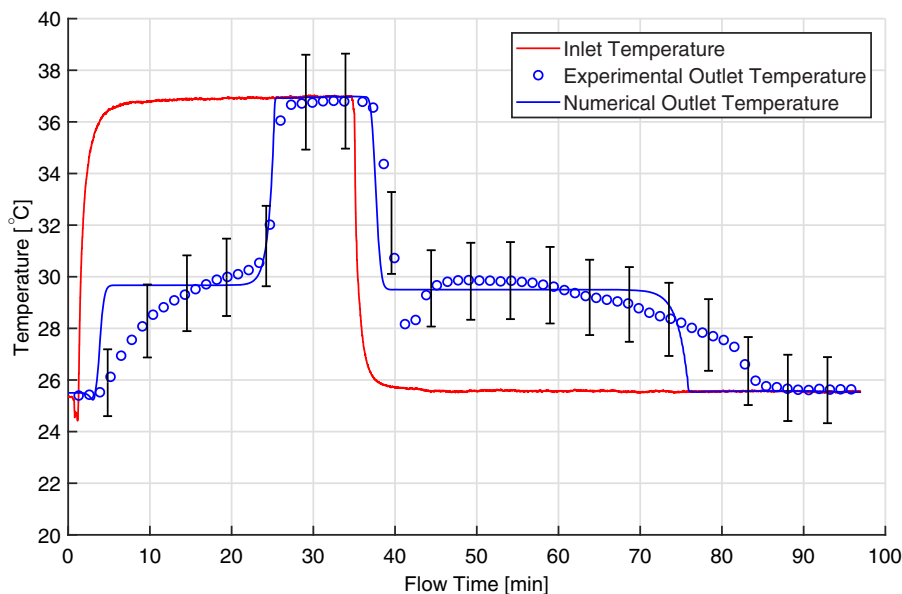|	N_{tu}	R_{we}	St_{io}
Run 1 Ext	32.4	0.534	0.234
Run 1 Char	31.2	0.541	0.234
Run 2 Ext	32.5	0.534	0.234
Run 2 Char	30.4	0.541	0.234

Fig. 4 Complete melting and freezing: Run 1. Inlet temperature ranges from 37 °C to 25 °C through the consecutive melting and freezing processes. The model predicted outlet temperature (solid line) is compared with experimental measurements (open circles).
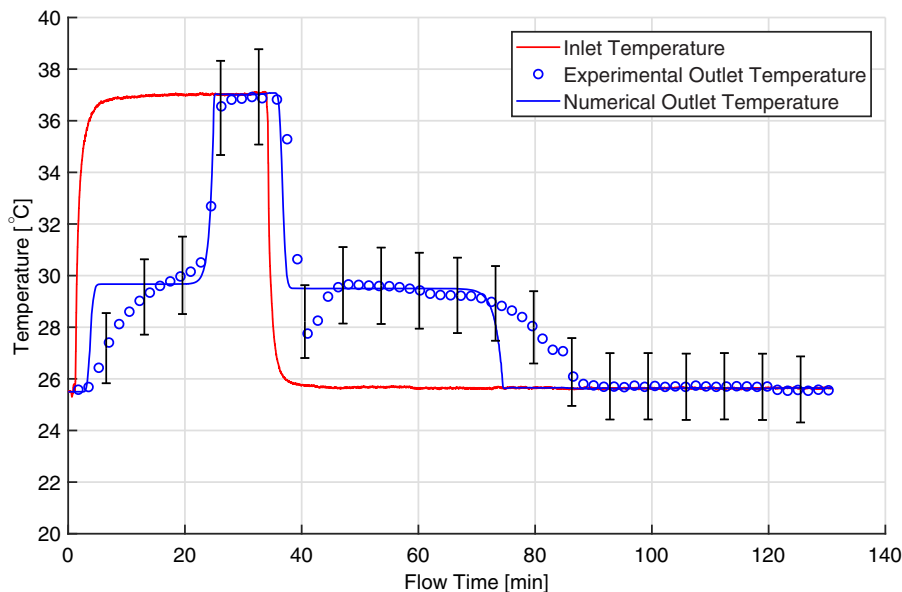

Fig. 5 Complete melting and freezing: Run 2. Inlet temperature ranges from 37 °C to 25 °C through the consecutive melting and freezing processes. The model predicted outlet temperature (solid line) is compared with experimental measurements (open circles).

comparison to the numerical model. For the complete melting and freezing tests, the flow direction matched configuration B as previously shown in Fig. 2, with both flows in the same direction. Run 2, with transient inlet and outlet temperatures reproduced in Fig. 5, generated similar results to Run 1 shown in Fig. 4. Both of these figures present the comparison of experimental and numerical inlet and outlet temperature measurements. The error bars depict experimental uncertainty and serve to highlight how well the simulation predicts the results.

The metric used to determine whether or not the numerics effectively captures the physics is the process end time (e.g., time to melt and time to freeze). For Runs 1 and 2, the completion times summarized in Tables 10 and 11 were observed. We noticed that the percent difference in melting completion time is consistent across the two runs, while the difference in freezing time is more statistically significant. We suspect that additional subcooling in Run 2

is the source of this increase. The most effective way to improve the model would be to modify the governing equations to include subcooling of the PCM.

It is challenging to capture the exact heat transfer physics with the computational program. Aside from subcooling, we see other differences between the outlet temperature predicted by the model compared with the experimental data. We noted that the model slope is too steep, while the PCM is solid for melting and freezing, but that steep slope matches well, while the PCM is liquid for both processes. This inconsistency could be attributed to a difference in thermophysical properties ($c_s < c_l$, $k_s > k_l$, $\rho_s > \rho_l$) which impact both conductance (heat transfer) and capacitance (energy storage). The model currently uses constant average values, given in Table 2, for each of these thermophysical properties and does not account for the property variation between liquid and solid PCM. Despite this, the difference in thermophysical properties between the two
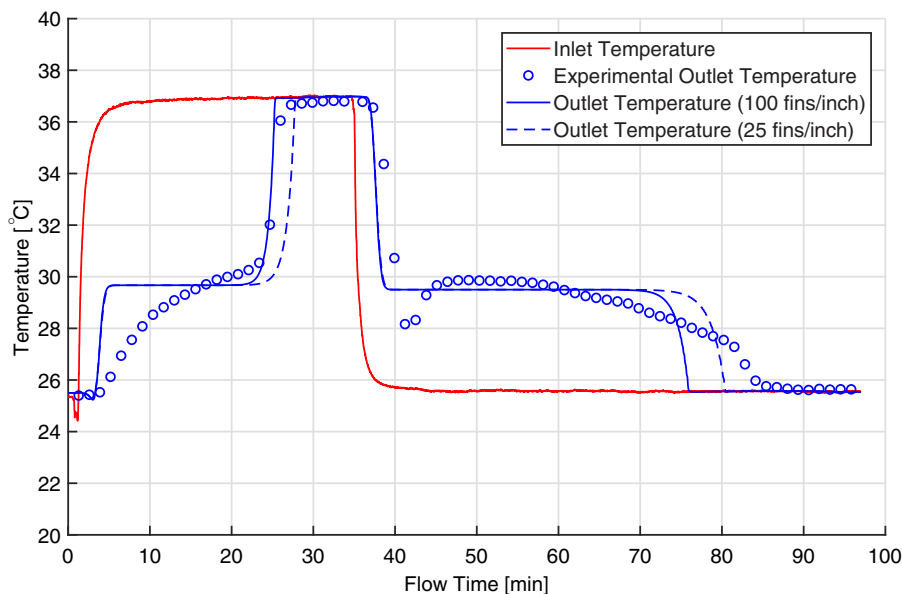
Fig. 6   Complete melting and freezing: Run 1 with slight design modifications

PCM states is fairly minimal. Another possibility is that there is additional thermal mass in the heat exchanger core that we are not accounting for. The metal casing that contains the PCM and maintains the integrity of the structure is most significant around the perimeter of the core; on the top, bottom, and sides. While this might be relevant, we estimate that the 5 mm thick perimeter casing would contribute an additional 0.86 kg of aluminum with a small capacitance compared with the latent energy storage available with the PCM. This likely makes minimal difference in the model predictions, though we will explore it in future work. We believe that the model disagreement is more likely due to a major contact resistance between the flow channel and PCM that is present when the salt hydrate is dehydrated. We are currently creating another PCM heat exchanger model to test this hypothesis.

This disagreement predicted by our preliminary first-principles model falls mostly within the uncertainty associated with temperatures measured in the experiment. Where the numerical prediction does not fall within error bars, the absolute difference between experimental measurement and numerical prediction is around 1–2 °C. This lends significant support to the accuracy of the model prediction. Even more importantly, the process completion time is quite close, ranging between 4 and 18% difference. The highest discrepancy is observed during freezing. There, the numerical program is not designed to capture the poor nucleation

rates (at ∼40 min) before the phase change material can start freezing. We plan to improve the numerical program by including a model for subcooling that can predict these effects and hopefully bring the percent difference of freezing closer to that of melting.

Due to the reasonable accuracy with which the computational model can be used to predict process completion times, it can be used as a highly efficient and cheap design tool. For example, the number of fins per inch within the storage matrix sections can be reduced, thereby increasing the void fraction, and decreasing the overall heat transfer coefficient. To maintain a consistent amount of energy storage capacity, the height of the storage matrix sections can be reduced, resulting in the same amount of PCM in the TES device. The conductance associated with this proposed design is enumerated in Table 12.

The result of this reduction in metal in the storage matrix is shown here. As evidenced by Fig. 6, the melting and extraction processes take only slightly longer than their 100 fins/in. counterpart prediction. This indicates that a cheaper design, using 1/4 of the metal in the storage matrix, would still produce a TES device that performs within the desired time.

Conclusions

The work discussed in this paper demonstrates experimental validation of a first-principles model for high-performance TES designs.

We presented a summary of experimental tests of a TES unit with lithium nitrate trihydrate phase change material as a storage medium. The presented performance data are for complete dual-mode cycles consisting of extraction and charging. The model analysis is found to agree reasonably well with experiments, within 5% for melting and within 18% for freezing. Higher percent deviation with the experimental data is attributed to conditions very near the initiation of freezing. This is a consequence of subcooling that is required to initiate solidification. Additional modifications could be included to capture the physics of subcooling within the numerical model

Table 10   Time to complete processes: Run 1

Experimental melting completed:	27.0	min
Numerical melting completed:	25.8	min
Percent difference	4.42	%
Experimental freezing completed:	85.2	min
Numerical freezing completed:	76.5	min
Percent difference	10.7	%

Table 11   Time to complete processes: Run 2

Experimental melting completed:	26.5	min
Numerical melting completed:	25.5	min
Percent difference	3.85	%
Experimental freezing completed:	89.5	min
Numerical freezing completed:	74.8	min
Percent difference	17.8	%

Table 12   Overall heat transfer coefficient, $\overline{U}$

	25 fins/in.	100 fins/in.	
Run 1 Extraction	2520	2990	W/(m^2 K)
Run 1 Charging	2440	2880	W/(m^2 K)

and consideration of secondary modes that change the PCM heat exchanger's conductance (contact resistance) and capacitance (sensible storage). While improvements could be made, this research effectively simulates and validates spatial and temporal variation within a TES device. The strength of this work is that it demonstrates close agreement with a model through the stages of the melting and freezing processes for a storage technology designed to work efficiently in a limited time window. We hope that the field can benefit from the experimentally validated model presented here. Accurately predicting the working fluid temperature exiting a PCM heat exchanger will be highly valuable for many more applications, as we electrify heating and shift to a renewable power grid.

Nomenclature

h = convective heat transfer coefficient
j = numerical spatial index
n = numerical temporal index
s = spacing between offset fins
u = experimental measurement uncertainty
$\dot{m}$ = working fluid mass flowrate per passage
E = energy transferred into the TES
L = length of the TES device
U = overall heat transfer coefficient
$c_{p,m}$ = specific heat of the metal mesh
$c_{p,\mathrm{PCM}}$ = specific heat of the PCM
$c_{p,s}$ = effective specific heat of the storage matrix
$c_{p,w}$ = specific heat of the working fluid
h_f = height of offset fin
h_{ls} = latent heat of fusion of the PCM in the storage matrix
k_m = thermal conductivity of the metal mesh
k_{PCM} = thermal conductivity of the PCM
k_s = effective thermal conductivity of the storage matrix
k_w = thermal conductivity of the working fluid
l_f = length of offset fin
n_s = number of storage matrix sections
n_w = number of working fluid flow passages
s_w = wetted perimeter of the working fluid flow passage
t_f = thickness of offset fin
x_e = melt fraction of a discrete element in the storage matrix
A_c = cross-sectional area of the working fluid flow passage
D_h = hydraulic diameter of the working fluid flow passage
$Ecap$ = energy storage capacity of the TES
N_{tu} = number of transfer units in TES
R_{we} = ratio of working fluid and storage matrix element thermal capacities
T_e = temperature of a discrete element in the storage matrix
T_m = melt temperature of the PCM in the storage matrix
T_{max} = maximum temperature encountered in the TES device
T_{min} = minimum temperature encountered in the TES device
T_w = temperature of a discrete parcel of working fluid
T_{wi} = inlet temperature of the working fluid
Nu = Nusselt number
Pr = Prandtl number
Re = Reynolds number
St_{io} = Stefan number between the inlet and outlet of the TES
Sta = Stanton number
Δt^* = non-dimensional temporal discretization
$\Delta z^\wedge$ = non-dimensional spatial discretization
ε_{exp} = experimental effectiveness of the TES
ε_s = fraction of the storage matrix occupied by PCM
ε_{tes} = heat transfer effectiveness of the TES
η_{fin} = offset fin efficiency
θ = dimensionless temperature of a discrete element in the storage matrix
θ_m = dimensionless melt temperature of the PCM
ν' = storage matrix volume per unit length of the device
ρ_m = density of the metal mesh
ρ_{PCM} = density of the PCM
ρ_s = effective density of the storage matrix
ρ_w = density of the working fluid
φ = dimensionless temperature of a discrete parcel of working fluid
φ_{wi} = dimensionless inlet temperature of the working fluid

Conflict of Interest

There are no conflicts of interest.

References

[1] Shamsundar, N., and Srinivasan, R., 1980, "Effectiveness-NTU Charts for Heat Recovery From Latent Heat Storage Units," ASME J. Sol. Energy Eng., **102**(4), pp. 263–271.
[2] Bellecci, C., and Conti, M., 1993, "Transient Behaviour Analysis of a Latent Heat Thermal Storage Module," Int. J. Heat Mass Transfer, **36**(15), pp. 3851–3857.
[3] Ismail, K., and Goncalves, M., 1999, "Thermal Performance of a PCM Storage Unit," Energy Convers. Manage., **40**(2), pp. 115–138.
[4] Alkilani, M., Sopian, K., Mat, S., and Alghoul, M., 2009, "Output Air Temperature Prediction in a Solar Air Heater Integrated With Phase Change Material," Eur. J. Sci. Res., **27**(3), pp. 334–341.
[5] Tay, N., Belusko, M., and Bruno, F., 2012, "An Effectiveness-NTU Technique for Characterising Tube-in-Tank Phase Change Thermal Energy Storage Systems," Appl. Energy, **91**(1), pp. 309–319.
[6] Bony, J., and Citherlet, S., 2007, "Numerical Model and Experimental Validation of Heat Storage With Phase Change Materials," Energy Build., **39**(10), pp. 1065–1072.
[7] Hosseini, M., Rahimi, M., and Bahrampoury, R., 2015, "Thermal Analysis of PCM Containing Heat Exchanger Enhanced With Normal Annular Fines," Mech. Sci., **6**(2), pp. 221–234.
[8] Wu, J., Tremeac, B., Terrier, M.-F., Charni, M., Gagnière, E., Couenne, F., Hamroun, B., and Jallut, C., 2016, "Experimental Investigation of the Dynamic Behavior of a Large-Scale Refrigeration—PCM Energy Storage System. Validation of a Complete Model," Energy, **116**(1), pp. 32–42.
[9] Waser, R., Ghani, F., Maranda, S., O'Donovan, T., Schuetz, P., Zaglio, M., and Worlitschek, J., 2018, "Fast and Experimentally Validated Model of a Latent Thermal Energy Storage Device for System Level Simulations," Appl. Energy, **231**(1), pp. 116–126.
[10] Sun, X., Mo, Y., Li, J., Chu, Y., Liu, L., and Liao, S., 2020, "Study on the Energy Charging Process of a Plate-Type Latent Heat Thermal Energy Storage Unit and Optimization Using Taguchi Method," Appl. Therm. Eng., **164**(1), p. 114528.
[11] Helmns, A., and Carey, V. P., 2016, "Modeling of Heat Transfer and Energy Efficiency Performance of Transient Cold Storage in Phase Change Thermal Storage Components," ASME 2016 Heat Transfer Summer Conference, Washington, DC, July 10–14, American Society of Mechanical Engineers, p. V001T05A009.
[12] Helmns, A., and Carey, V. P., 2017, "Modeling of Intramatrix Heat Transfer in Thermal Energy Storage for Asynchronous Cooling," ASME 2017 Heat Transfer Summer Conference, Bellevue, WA, July 9–12, American Society of Mechanical Engineers, p. V001T09A006.
[13] Theroff, Z. M., Helmns, D., and Carey, V. P., 2018, "Exploration of Variable Conductance Effects During Input and Extraction of Heat From Phase Change Thermal Storage," ASME 2018 International Mechanical Engineering Congress and Exposition, Pittsburgh, PA, Nov. 11–14, American Society of Mechanical Engineers.
[14] Helmns, A., and Carey, V. P., 2018, "Multiscale Transient Modeling of Latent Energy Storage for Asynchronous Cooling," ASME J. Therm. Sci. Eng. Appl., **10**(5), p. 051004.
[15] Gagnon, L. B., Helmns, D., and Carey, V. P., 2018, "Multiscale Modeling of Power Plant Performance Enhancement Using Asynchronous Thermal Storage and Heat Rejection," ASME 2018 International Mechanical Engineering Congress and Exposition, Pittsburgh, PA, Nov. 11–14, American Society of Mechanical Engineers.
[16] Gagnon, L., Helmns, D., and Carey, V. P., 2020, "Multiscale Modeling of Power Plant Performance Enhancement Utilizing Asynchronous Cooling With Thermal Energy Storage," ASME J. Heat Transfer, **142**(5), p. 052905.
[17] Kumar, N., and Banerjee, D., 2018, "Phase Change Materials," Handbook of Thermal Science and Engineering, Springer International Publishing, Cham, Switzerland, pp. 2213–2275.
[18] Shamberger, P. J., and Reid, T., 2012, "Thermophysical Properties of Lithium Nitrate Trihydrate From (253 to 353) K," J. Chem. Eng. Data, **57**(5), pp. 1404–1411.
[19] Kumar, N., and Banerjee, D., 2018, "A Comprehensive Review of Salt Hydrates as Phase Change Materials (PCMs)," Int. J. Transp. Phenom., **15**(1), pp. 65–89.
[20] Meseguer, J., Pérez-Grande, I., and Sanz-Andrés, A., 2012, Spacecraft Thermal Control, Elsevier, New York.